From Topographic Internal Gravity Waves to Turbulence

S. Sarkar[1] and A. Scotti[2]

[1]Department of Mechanical and Aerospace Engineering, University of California, San Diego, La Jolla, California 92093; email: ssarkar@ucsd.edu

[2]Department of Marine Sciences, University of North Carolina at Chapel Hill, Chapel Hill, North Carolina 27599

Annu. Rev. Fluid Mech. 2017. 49:195–220

First published online as a Review in Advance on July 22, 2016

The *Annual Review of Fluid Mechanics* is online at fluid.annualreviews.org

This article's doi: 10.1146/annurev-fluid-010816-060013

Keywords

turbulence, internal waves, rough topography, mixing

Abstract

Internal gravity waves are a key process linking the large-scale mechanical forcing of the oceans to small-scale turbulence and mixing. In this review, we focus on internal waves generated by barotropic tidal flow over topography. We review progress made in the past decade toward understanding the different processes that can lead to turbulence during the generation, propagation, and reflection of internal waves and how these processes affect mixing. We consider different modeling strategies and new tools that have been developed. Simulation results, the wealth of observational material collected during large-scale experiments, and new laboratory data reveal how the cascade of energy from tidal flow to turbulence occurs through a host of nonlinear processes, including intensified boundary flows, wave breaking, wave-wave interactions, and the instability of high-mode internal wave beams. The roles of various nondimensional parameters involving the ocean state, roughness geometry, and tidal forcing are described.

1. INTRODUCTION

Barotropic tide: oscillatory motion that is in phase across the entire water column and driven by lunar and solar gravitation forces

Internal gravity waves are ubiquitous in the stratified, rotating ocean. Similar to the more familiar surface waves, internal waves transport momentum and energy over large distances in the open ocean. However, a crucial difference between the two types of waves is that internal waves span the entire vertical stratification of the water column. The linear dynamics of these waves is distinctive (see the sidebar The Dispersion Relationship for Internal Waves and **Figure 1**). When nonlinear effects become sufficiently strong, wave energy cascades into instabilities and turbulence. With the exception of waves in the inertial band, which are predominantly wind forced, oceanic internal waves are mainly generated by the tide oscillating over rough features on the ocean floor, such as ridges, seamounts, and canyons. Topographic waves can have much larger vertical and horizontal fluid velocities in the deep ocean than the generating barotropic tide, making them susceptible to nonlinear effects. An extreme example is provided by the South China Sea, where powerful waves with observed vertical displacements up to 500 m and horizontal fluid velocity up to 1.5 m/s are generated at the double-ridge system of Luzon Strait and flux energy away at a rate of approximately 15 GW (Alford et al. 2015).

Through their associated velocities and turbulence, internal waves impact ocean processes cutting across a large swath of spatial and temporal scales, as well as many subdisciplines. These

THE DISPERSION RELATIONSHIP FOR INTERNAL WAVES

Linearizing the Euler equations under the Boussinesq approximation in a frame rotating at angular velocity $f/2$ (half the Coriolis frequency), and assuming constant stratification N (with N the buoyancy frequency or the Brunt-Väisälä frequency), yields a wave equation that admits solution in the form of plane waves. The special case $N = 0$ gives rise to what is known in the Russian literature as the Sobolev equation (Sobolev 1955). In the frame of reference where y-z is the plane that contains the wave vector $\mathbf{k} = (0, l, m) = K(0, \cos\Phi, \sin\Phi)$, the dispersion relationship linking frequency ω to the wave number is given by

$$\omega^2 = N^2 \cos^2\Phi + f^2 \sin^2\Phi.$$

Unlike standard waves, where the frequency is a function of the magnitude K of the wave number, the internal wave frequency is set by the angle of propagation. A simple manipulation shows that the group velocity is orthogonal to the phase velocity. Hence, Φ is the angle of the phase velocity with the horizontal plane and the angle of the group velocity with the vertical axis. Given the invariant nature of the equations under rotations around the vertical axis, the group velocity of internal waves generated by a pointwise source oscillating at frequency ω is constrained to lie on a cone (the group velocity cone; see **Figure 1**) whose vertex is centered on the source and whose opening angle is 2Φ, where

$$\tan^2\Phi = \frac{N^2 - \omega^2}{\omega^2 - f^2}.$$

Note that the above equation requires that $f \le \omega \le N$. Because f increases with latitude, propagating waves with periods longer than 12 h are confined to a latitudinal band. Thus, the internal M2 tide (period 12.4 h) is confined between −74.5S and 74.5N, whereas the internal K1 tide (period 23.92 h) exists between −30.1S and 30.1N. In most oceans, N is greater than most tidal frequencies, with the exception of a few very weakly stratified abyssal regions. The angle of the phase line (also the group velocity) with the horizontal plane is $\alpha = \pi/2 - \Phi$ and satisfies

$$\tan\alpha = \sqrt{\frac{\omega^2 - f^2}{N^2 - \omega^2}} = \frac{\omega}{N}\sqrt{\frac{1 - (f/\omega)^2}{1 - (\omega/N)^2}}.$$

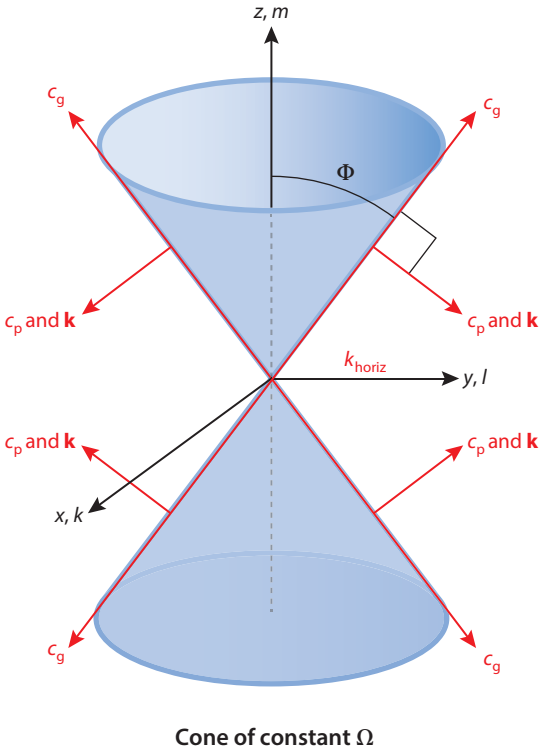

Figure 1

Schematic illustration of the geometry of linear internal wave propagation. Waves originating from a pointwise source at the apex of the cone radiate energy along the surface of the cone. The wave number **k** and phase velocity c_p are normal to the surface of the cone. The group velocity, c_g, is parallel to the surface of the cone.

ocean processes bear on shipping, underwater navigation, renewable energy, offshore oil drilling, fisheries, and weather, as well as present and future climate states. Turbulent mixing driven by internal waves was long ago recognized as one of the key factors that control the meridional overturning circulation (see, e.g., the review of Wunsch & Ferrari 2004, and references therein), and predictions of ocean circulation are sensitive to both the magnitude and vertical distribution of wave-driven mixing (Saenko 2005, Jayne 2009, Melet et al. 2013). On much shorter timescales, these waves transport nutrients, pollutants, and sediments and thereby impact local biology (Leichter et al. 2003, Wong et al. 2012) and geomorphology (Cacchione et al. 2002, McPhee-Shaw 2006). Through their structural loads, internal waves present hazards for offshore structures and submerged vehicles (Osborne et al. 1978).

Topographic internal waves are a key contributor to the diapycnal mixing necessary to maintain the observed oceanic stratification in the abyssal ocean (deeper than 1,000 m) (Wunsch & Ferrari 2004). A simple one-dimensional (1D) balance between upward advection of cold water formed at high latitudes and downward diffusion of heat yields a basin-averaged value of thermal diffusivity, $K_T \sim 10^{-4}$ m^2/s (Munk & Wunsch 1998), approximately three orders of magnitude larger than the molecular value. Observations of such large values of K_T in the abyssal ocean are limited for the most part to water over rough topography. Tidal forcing is the crucial energy source for the enhanced diffusivity. Approximately 1 TW is converted globally from the barotropic tide to

internal waves at rough deep topography according to satellite altimeter data (Egbert & Ray 2001). Some of the wave energy dissipates over complex topography during generation, leading to local turbulent mixing, while the remainder radiates away, providing a reservoir for remote mixing during wave propagation, interaction with ocean currents, eddies, and nonuniform stratification, as well as reflection at other topographic features.

We review progress made during the past 5–10 years in characterizing the nonlinear breakdown of topographic internal waves, in quantifying the resulting turbulence, and in connecting small- and large-scale processes. Some recent reviews in this journal have touched on issues relevant to the present discussion, notably Garrett & Kunze (2007) on generation process with an emphasis on linear theory and Ivey et al. (2008) on mixing in stratified flow by shear-driven turbulence. The case of internal solitary wave (ISW) breaking on the continental shelf/slope has been extensively reviewed by Lamb (2014) and is therefore excluded here.

2. GENERATION OF INTERNAL WAVES BY TIDAL FLOW

When a surface tide with maximum velocity U_0 and frequency Ω oscillates over a topographic feature with height h and length $2l$, it sets up an oscillatory vertical velocity with maximum amplitude $U_0 \mathrm{d}h/\mathrm{d}x$ at the boundary. This oscillatory boundary forcing leads to propagating internal gravity waves if $f < \Omega < N$, where f is the Coriolis parameter and N is the buoyancy frequency. The wave phase line (also group velocity) makes an angle α with the horizontal plane (see the sidebar The Dispersion Relationship for Internal Waves). Typically, tidally forced waves have $\Omega/N \ll 1$ because the tidal forcing has a period of several hours (e.g., the M2 tide with a period of 12.4 h), much larger than the buoyancy time period, which, with some exceptions, ranges between 15 min and 1 h. This leads to $\tan(\alpha) \simeq (\Omega/N)\sqrt{1-(f/\Omega)^2} \leq \Omega/N$. Thus, a wave with M2 tidal period propagates at a shallow angle in the midwater column (e.g., 4–8° when $N = 0.002$–$0.001\ \mathrm{s}^{-1}$). If the barotropic tide is subinertial ($\Omega < f$) as can occur at sufficiently high latitude, internal waves cannot propagate (e.g., the M2 tide becomes subinertial for latitudes exceeding 74.5°).

Table 1 lists the nondimensional parameters that govern wave generation by a topographic feature, with the excursion number (Ex), steepness (γ), and local slope criticality (ϵ) being particularly important. The excursion number, $Ex = U_0/\Omega l$, is the ratio of net fluid advection by the barotropic tide to the topographic length and is a measure of nonlinearity. The parameter Ex is generally small for large generation sites but can be large for smaller topographic features. An M2 tide with an amplitude of 0.2 m/s has an advection length scale, 1.4 km. Topography with $l = 100$ km corresponds to a small $Ex = 0.014$, whereas a small feature with $l = 1.4$ km corresponds to $Ex = 1$. The steepness parameter is $\gamma = (h/l)/\tan\alpha$ and distinguishes among subcritical ($\gamma < 1$), critical ($\gamma = 1$), and supercritical ($\gamma > 1$) slope. Steep topography refers to $\gamma \geq 1$ (i.e., in some locations the average slope angle is larger than the wave propagation angle, α). Because $\alpha \sim 3$–8°, ocean roughness can be dynamically steep even with a geometrically moderate slope.

2.1. Linear Theory

Linear theory for wave generation by the oscillating tide has been extensively reviewed by Garrett & Kunze (2007). Briefly, Bell (1975) examined the problem using the so-called weak topography approximation based on a shallow slope, $\gamma \ll 1$, and topography height much less than the vertical wavelength of the internal tide. The theory has been developed further by others (e.g., Llewellyn Smith & Young 2002, Pétrélis et al. 2006) to address more realistic cases with steeper slope and larger topographic height. Linear theory gives the conversion from barotropic to internal wave

Table 1 Dimensional and nondimensional parameters of internal wave generation by tidal flow over an obstacle

	Parameter	Symbol (unit)
Geometry	Obstacle height	h (m)
	Obstacle length	$2l$ (m)
	Critical slope length	$2l_{cr}$ (m)
	Local slope angle	β (°)
Tidal forcing	Amplitude	U_0 (m/s)
	Frequency	Ω (s^{-1})
Environment	Buoyancy frequency	N (s^{-1})
	Coriolis parameter	f (s^{-1})
	Wave propagation angle	$\alpha = \text{atan}\sqrt{\frac{\Omega^2 - f^2}{N^2 - \Omega^2}}$ (°)
	Ocean depth	H (m)
Fluid properties	Kinematic viscosity	ν (m^2/s)
	Thermal diffusivity	κ (m^2/s)
Nondimensional	Excursion number	$Ex = U_0/\Omega l$
	Topographic steepness	$\gamma = h/l \tan\alpha$
	Relative height	h/H
	Rotation	Ω/f
	Slope criticality	$\epsilon = \tan\beta/\tan\alpha$
	Topographic Froude number	$Fr_h = U_0/Nh$
	Fraction of critical slope	l_{cr}/l
	Reynolds number	$Re = U_0^2/\Omega\nu$
	Reynolds number (response)	$Re = U\delta/\nu$
Flow response	Horizontal fluid velocity	U
	Vertical scale	δ
	Reynolds number	$U\delta/\nu$
	Gradient Richardson number	$Ri = N^2\delta^2/U^2$
	Horizontal phase velocity of wave	c_p
	Wave Froude number	$Fr_w = U/c_p$

energy (also the radiated power per unit span of the obstacle in the linear, inviscid approximation) as

$$C = \bar{C}\rho_0 U_0^2 h^2 \sqrt{N^2 - \Omega^2}, \quad (1)$$

where the proportionality coefficient $\bar{C}$ depends on the geometry of the topography through nondimensional parameters listed in **Table 1**. In particular, $\bar{C}$ is much larger for steep obstacles with $\gamma > O(1)$ than for obstacles with gentle slope. The expression for C derived from linear theory is important both as a quantitative estimate (likely an upper bound) of the parameterized wave energy flux in global climate models and as a scaling law for the dependence of energy conversion on tidal amplitude, obstacle height, and stratification.

Baroclinic or internal tide: oscillatory motion that has vertical structure owing to vertical density stratification; an internal wave forced by the barotropic tide flowing over bottom topography

2.2. Nonlinearity

Let us consider the near-field wave pattern generated at a symmetric 2D obstacle shown in **Figure 2**. The subcritical case with gentle slope shown in **Figure 2*a*,*b*** is one where the near field is approximately linear: The isopycnals do not steepen, and the baroclinic velocity is not large. Note that the subcritical slope is gentle but appears not to be so in the figure because of the different normalizations used for topographic height and width. When $Ex \ll 1$, the wave field

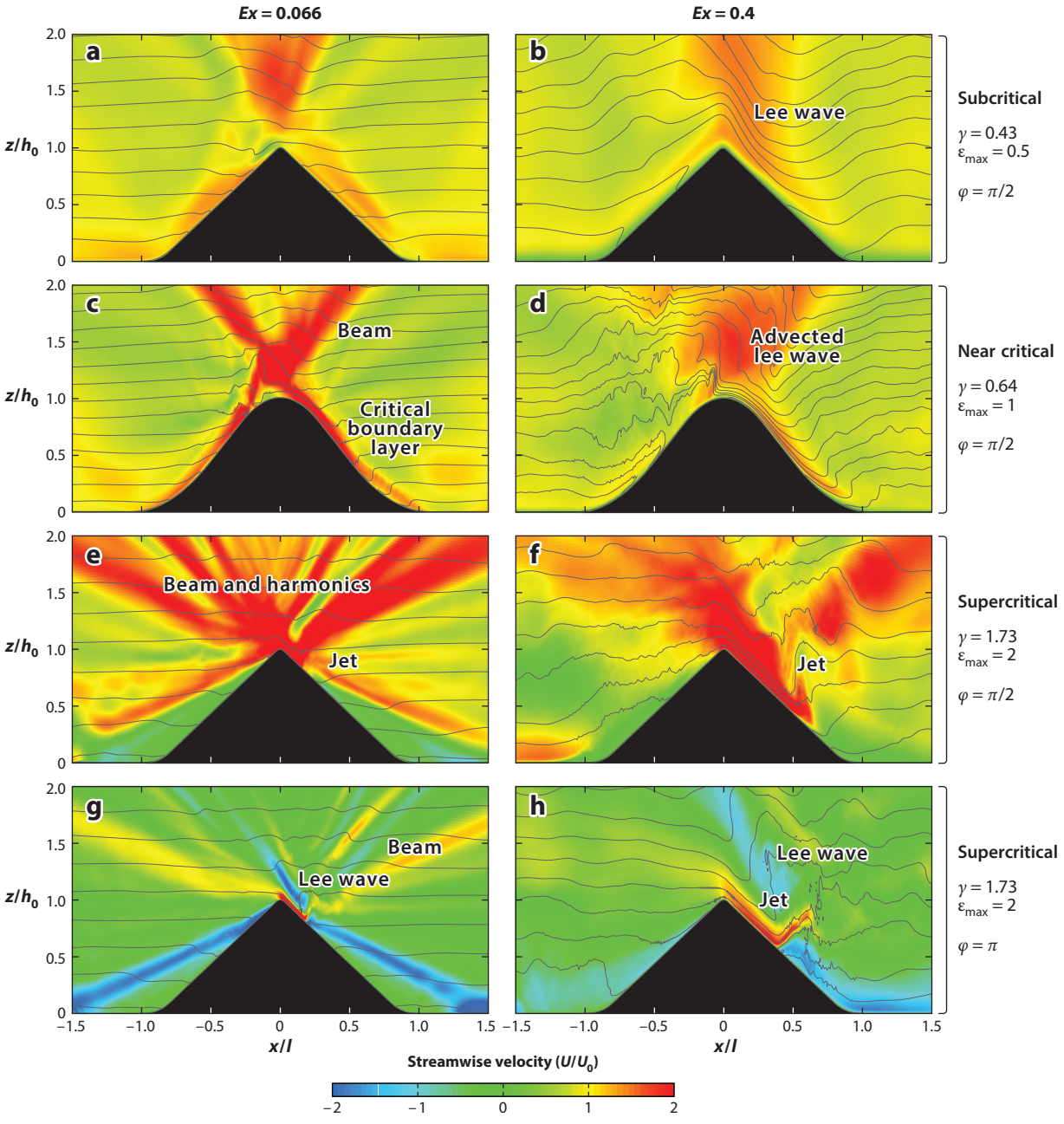

Figure 2

Flow response at a model triangular obstacle to an oscillating tide. Contours of streamwise velocity U/U_0 are shown in color, and isopycnals are represented as gray lines. The top three rows show the phase of maximum positive (rightward) velocity ($\phi = \pi$), and the bottom row shows zero ($\phi = \pi/2$) velocity when the flow reverses from down- to upslope. Note that the horizontal and vertical axes are normalized with the corresponding obstacle length scales so that the obstacle slope is distorted to 1:1 in the plot from a smaller value.

is nearly symmetric at all phases; furthermore, for subcritical topography, the wave energy leaves the obstacle in the form of symmetric beams that make an angle α with the horizontal plane, and the wave energy resides in the fundamental frequency, Ω. When the steepness γ increases to 1 and beyond in this low-Ex regime, the internal wave beam becomes thinner and the boundary fluid velocity, U_b, intensifies. With increasing Ex, the beam pattern shifts to the lee of the obstacle, and the beams lose their coherence, as seen for the cases with $Ex = 0.4$. When $Ex \geq O(1)$, lee waves are launched during the high-velocity stage, the oceanic analog of mountain waves. The lee waves have wavelength $2l$ and frequency $\omega = U_0\pi/l$ that radiate if $f < \omega < N$. Nonlinear effects can occur in the regime of small topographic Froude number, $Fr_h = U_0/Nh < O(1)$. U_0/N is important from energy considerations given that, in a stratified fluid, a particle with velocity U_0 has sufficient energy to overcome the potential energy barrier of vertical displacements up to U_0/N.

Internal wave beam: an internal wave field obtained by the superposition of plane waves with the same frequency and wave numbers **k** whose orientation is fixed (set by the frequency) and varying magnitude

In the case of a steady current with $Fr_h < O(1)$, there are nonlinear hydraulic effects (Baines 1995): blocking of flow in the bottom layer deeper than $O(U_0/N)$ from the crest, acceleration of the flow at the crest leading to a thin fast-moving layer with $Fr = O(1)$, and transition to subcritical flow in the lee through a hydraulic jump. Flow acceleration at the ridge crest and downslope jets also occur in oscillatory flow in the case of steep, supercritical topography (Winters & Armi 2013) and are illustrated in **Figure 2*b*** for $Ex = 0.4$.

Fr_h and Ex are not independent parameters (e.g., $Fr_h = Ex/\gamma$ for a triangular obstacle). For general topography, one finds $Fr_h \sim Ex/\gamma$ if the local slope angle is mostly $O(h/l)$; therefore, tidal flow in the regime of $Ex < O(1)$ and $\gamma = O(1)$ admits the possibility of a nonlinear hydraulic response at the upper portion of the ridge. Using 2D nonhydrostatic simulations of tidal flow over Kaena Ridge (a tall steep obstacle), Legg & Klymak (2008) showed that lee waves form, are subsequently released when the flow reverses from down- to upslope, and lead to steep isopycnals as they propagate upslope. Winters & Armi (2013) introduced an inner horizontal length scale, l_{in}, of the unblocked upper region of the obstacle that corresponds to the vertical distance U_c/N below the ridge crest. Here, $U_c > U_0$ is the accelerated crest velocity. The inner excursion number was defined as $Ex_{\text{in}} = U_c/(\Omega l_{\text{in}})$, and it was hypothesized that a nonlinear response occurs if $Ex_{\text{in}} = O(1)$. For a triangular obstacle of slope h/l, it follows that

$$l_{\text{in}} = \frac{U_c}{N}\frac{l}{h} \quad \Longrightarrow \quad Ex_{\text{in}} = \frac{U_0}{\Omega l_{\text{in}}} = \frac{U_0}{U_c}\frac{h/l}{\Omega/N} = \gamma/I, \tag{2}$$

where $I = U_c/U_0$ is the intensification of the velocity at the ridge crest. Thus, an obstacle that is steep [$\gamma \geq O(1)$] has $Ex_{\text{in}} \geq O(1)$ and, according to the hypothesis of Winters & Armi (2013), exhibits a nonlinear response at the ridge top even for small Ex, as found numerically for Kaena Ridge by Legg & Klymak (2008).

The internal wave beams apparent for the critical and supercritical cases in **Figure 2** have small vertical thickness and propagate vertically (for a definition of criticality in this context, see the sidebar Degeneracy and Critical Slopes; see also **Figure 3**). In the supercritical case, there are two upgoing and two downgoing beams. Vertically propagating beams were first observed in laboratory experiments (e.g., the famous St. Andrew's Cross); similarly, simulations show beams radiating from critical points. In the ocean, Pingree & New (1992) observed internal wave beams in the Bay of Biscay. Internal wave beams at the M2 frequency have been observed to originate from Kaena Ridge in Hawaii, and their structure has been studied (e.g., Cole et al. 2009).

In the case of steep topography, the internal wave field presents a rather complex picture with beams at various angles. Although much of the wave energy resides in the fundamental frequency, it is possible for the energy to leak into superharmonics with frequency $n\Omega$ and integer n when Ex increases owing to advection of the wave field by the barotropic tide (Bell 1975). In the case

DEGENERACY AND CRITICAL SLOPES

The dispersion relation is not the only unusual property of internal waves. For oscillating solutions of the form $\mathcal{S} = e^{i\omega t} q(\mathbf{x})$, where $\mathcal{S}$ is the full state vector (velocity and buoyancy), the resulting problem for $q(\mathbf{x})$ is hyperbolic in the space variables, rather than the more familiar elliptic problems that one encounters for standard wave equations (Sobolev 1955, Arnold & Khesin 1998). From a physical point of view, if a section of the physical boundary is tangent to the local group velocity cone (i.e., the slope is critical), the theory in frequency space breaks down, although the wave equation can still be solved in the time domain (Scotti 2011). The reader may at this point wonder if critical slopes are the norm or the exception in the ocean. **Figure 3** shows the difference $\Delta = \sin(\beta) - \sin(\Phi)$. The local slope angle β is obtained from a 1-min digital elevation model (but see Becker & Sandwell 2008 for a discussion on the importance of high-resolution bathymetry) and the wave propagation angle Φ from the dispersion relation setting $f = 2\Omega \sin(\theta)$, where Ω is Earth's angular velocity and θ the latitude angle, and using the ECCO2 data sets to calculate a climatology for N. Surprisingly, many areas, notably along continental slopes, are very close to criticality ($|\Delta| \ll 1$).

of a supercritical obstacle, the frequency spectrum shows superharmonic beams with frequency $n\Omega$ over the obstacle as well as away from the obstacle owing to the local spatial interaction of colliding beams, as shown in numerical results (Lamb 2004) and experiments (Peacock & Tabaei 2005, Zhang et al. 2007). Subharmonics with $\omega < \Omega$ are possible due to wave beam instability as well as interharmonics due to wave-wave interaction (Korobov & Lamb 2008). Subharmonics, superharmonics, and interharmonics are also found in flat-top topography with a finite length of critical slope, as shown using direct numerical simulation (DNS) by Gayen & Sarkar (2010), likely because of the interaction of the wave field with the intensified boundary velocity.

If a modal decomposition is applied to the internal wave field in the near field (that includes vertically thin beams) of a wave-generation site, the energy is found to be distributed over a wide range of modes. A single mode has horizontal phase propagation, but the sum of modes can also have vertical phase propagation. However, the far field is dominated by mode-1 or mode-2 energy in observations (e.g., Rainville & Pinkel 2006). Evidently, the high-mode waves are locally dissipated by nonlinear processes near the generation site. Additionally, the energy in the low mode is reduced by local dissipative processes, as shown numerically at a critical slope by Rapaka et al. (2013) and at a supercritical slope by Winters & Armi (2013). The laboratory experiment of Echeverri et al. (2009) also shows some decrease in energy across modes with increasing steepness and with increasing excursion number.

Mode-n internal wave: an internal wave whose vertical velocity field can be described as $w = A(x - c_n t)\phi_n(z)$, where $\phi_n(z)$ is the n-th eigenmode (with eigenvalue c_n) of the operator $\phi'' + (N/c_n)^2\phi = 0$

2.3. Observations

Measurements over seamounts (Kunze & Toole 1997, Lueck & Mudge 1997), submarine ridges (Polzin et al. 1997, Rudnick et al. 2003), submarine canyons (Carter & Gregg 2002, Wain et al. 2013), and the continental slope (Moum et al. 2002, Nash et al. 2007) show enhanced turbulence and mixing, likely driven by internal waves released by the tide oscillating over topography. Direct observational evidence for the tide → internal wave → turbulence cascade has been obtained through the Hawaiian Ocean Mixing Experiment (HOME) conducted at the 2,500-km-long Hawaiian Ridge, where tidal flow is approximately normal to the ridge (Rudnick et al. 2003, Klymak et al. 2006). Large depth-integrated fluxes of low-mode internal wave energy in the M2 band were measured at the Hawaiian Ridge and found in numerical models, and these

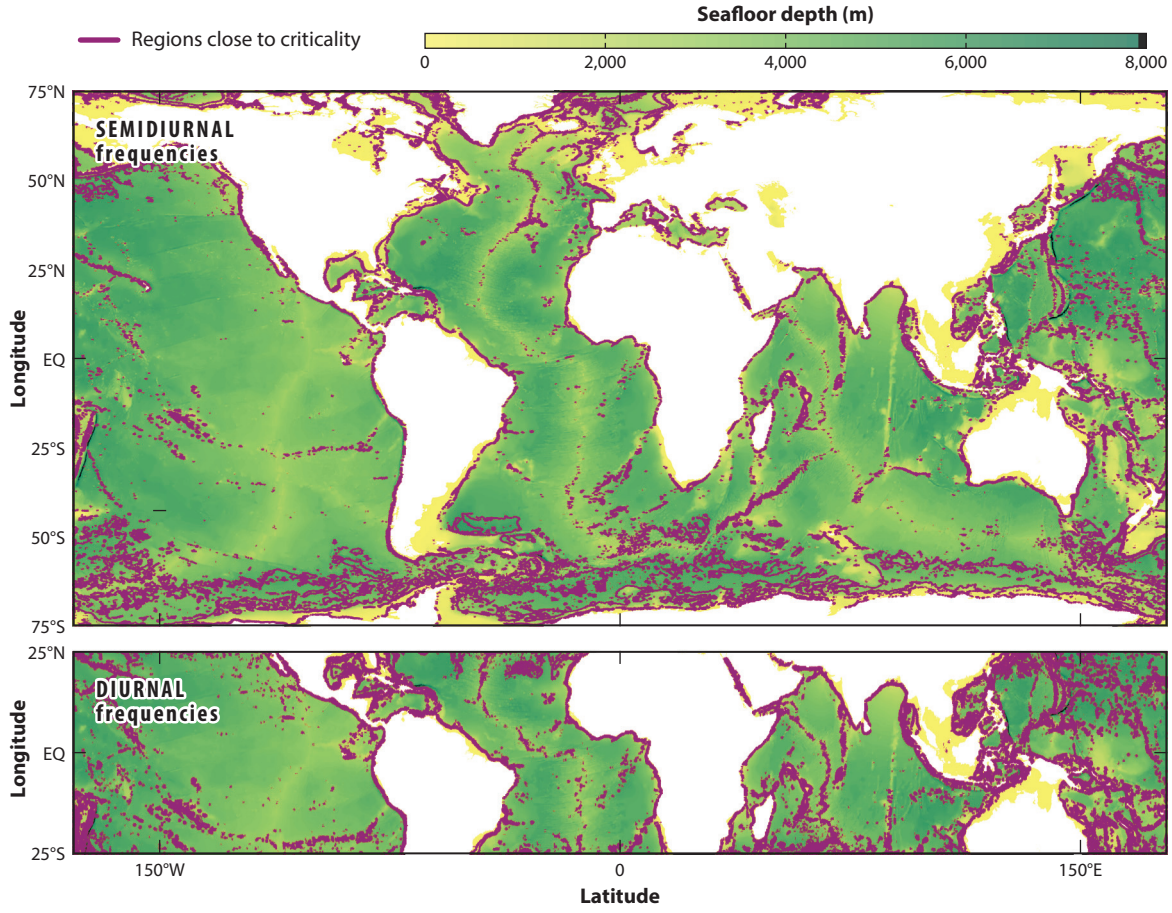

Figure 3

Criticality map at semidiurnal and diurnal frequencies showing the seafloor location (*color contours*) and regions close to criticality (*purple lines*), $|\Delta| \leq 1/20$. Here, Δ is the difference between the sine of the local slope and that of the angle of propagation of internal waves at the semidiurnal and diurnal frequencies. The topography is derived from the GEBCO One Minute Grid, version 2.0, and the stratification from the ECCO2 data sets (Menemenlis et al. 2008). Note that diurnal internal tides are limited to the equatorial band.

fluxes showed fortnightly modulation with the spring-neap cycle. Internal waves with displacements of up to 300 m were measured near the ridge top. Profiling, towed, and moored instruments showed bottom-intensified turbulent dissipation at the ridge top and at the deep ridge flanks, and 100-m-tall overturned patches with some evidence of phase locking with the barotropic tide. The inferred energy budget suggests that most of the internal tide energy radiates out as a low-mode internal tide from the Hawaiian Ridge with 15% or smaller energy dissipated locally. The recently concluded Internal Waves in the Straits Experiment (IWISE) examined the double-ridge system at Luzon Strait where the across-slope tides are more energetic than those along the Hawaiian Ridge, there are complex 3D features superposed on the two long ridges, and the internal tides radiating off the two ridges interact. Observations summarized by Alford et al. (2015) reveal rich dynamics: internal waves with extraordinarily large displacements up to 500 m, overturning patches as tall

as 300 m at the ridge system, wave refraction by the Kuroshio, and westward mode-1 waves that steepen dramatically to form solitary waves that break when they shoal onto the continental slope. Up to 40% of the energy is approximately estimated to dissipate locally.

Grid lepticity (λ): the ratio of horizontal grid resolution to an appropriate scale for vertical motions; the solution of the Poisson problem for the pressure p can be formally expanded as $p = \sum_{n=0}^{\infty} p_n \lambda^{-2n}$, with p_0 the hydrostatic pressure

3. NUMERICAL APPROACHES

Given the inherent difficulty and cost associated with in situ observations, numerical models have been extensively used to explore the barotropic-baroclinic coupling over topography. The choice of the model depends on where the split between resolved and unresolved scales falls. At the minimum, the horizontal resolution must be small enough to capture relevant topographic scales, as well as the scale of the internal tide. At high lepticity, the motion is hydrostatic, and a description based on the hydrostatic primitive equations is appropriate. Only when the lepticity is smaller than a $O(1)$ critical value is it necessary to switch to a nonhydrostatic formulation to reproduce accurately the physics (Scotti & Mitran 2008, Vitousek & Fringer 2011). Unfortunately, a nonhydrostatic simulation with a highly anisotropic 3D grid contains a badly conditioned elliptic problem, and standard iterative methods perform very poorly, making 3D nonhydrostatic computations in realistic settings extremely expensive (Santilli & Scotti 2011). Thus, the bulk of nonhydrostatic simulations involving the generation of internal waves have 2D simulations of 2D geometries (Legg & Klymak 2008, Buijsman et al. 2012). However, even when the large-scale topography is quasi-2D, 3D effects can be significant. For example, Buijsman et al. (2013) showed that the amplification of conversion in Luzon Strait is several times larger in 3D simulations even though the underlying topography is mostly 2D.

The onset of turbulence is often determined by 3D instabilities. If the focus is on the interplay between large-scale 2D forcing and turbulence, a promising approach is represented by large-eddy simulation (LES). The topography, idealized as 2D, is contained in a 3D domain. The depth along the third direction, and its discretization, must be chosen to capture the development of 3D instabilities. Although LES still needs to model the small unresolved turbulent scales, the latter have a more universal character, unlike turbulent parameterizations that need to account for the much less universal instabilities at the origin of the turbulent cascade. A challenge is to resolve turbulence while maintaining the correct geometric aspect ratio. There are few LES with realistic aspect ratios [e.g., the shallow angle (5°) slope considered by Gayen & Sarkar (2011b)]. LES is now being extended to realistic-shape topography with promising results [e.g., the 1:100 scaled-down model of a cross section of a Luzon ridge (Jalali et al. 2016)].

It is possible to nest a high-resolution model within a low-resolution ocean model, so that the latter can drive the former (e.g., Blayo & Debreu 2006, Debreu et al. 2012). This technique works best when the area that needs high resolution can be predicted a priori. Unfortunately, when dealing with internal waves over complex topography, turbulence may be intermittent in space and time. An active area of research is the development of models involving grids whose resolution can be dynamically adapted to accommodate evolving features. The models differ on the specific implementations. Some employ a finite-element discretization based on unstructured meshes (Piggott et al. 2008). Every so often, a new grid is generated, with the local density of elements determined by the character of the solution. The fields are then transferred from the old to the new grid, and the solution proceeds until the next regridding point is reached. This allows geometrical flexibility, but conservation of mass and momentum during the regridding step is a delicate issue. More recently, Santilli & Scotti (2015) developed a model based on a hierarchy of grids. Their approach is closer to the standard embedding of finer models within coarser ones, only in this case the grids are two-way coupled, and at any given level of the hierarchy, finer grids can be moved or added as needed. The model is based on a finite volume approach, which makes

transfer of information between grids easier. Also, it is easier to enforce continuity of fluxes across the fine-coarse interface. Embedding LES closure into this model is a topic of ongoing research.

4. TURBULENCE AT GENERATION SITES

The tidal velocity in deep water is usually small, and the turbulent boundary layer on a flat bottom dissipates a small [$O(10^{-3}$ W/m^2)] amount of energy. It is the nonlinear baroclinic response on sloping topography that leads to intensified fluid velocity, waves with small horizontal and vertical scales, and separated flows (**Figure 2**) leading to turbulence. Under conditions discussed below, the velocity U becomes sufficiently large, and the vertical scale δ of the flow becomes sufficiently small with the following possible outcomes: (*a*) The instantaneous stratification becomes locally unstable [$N^2(t) < 0$], resulting in transition to turbulence by convective instability. (*b*) The shear intensifies so that the local value of Ri decreases to less than the critical value of 0.25 so that there is shear instability. Both of the above outcomes become more likely for a boundary layer if the velocity is intensified and for a propagating wave when the fluid velocity U becomes comparable to the phase speed, c_p, so that the wave Froude number $Fr_w = U/c_p \sim O(1)$ (Baines 1995).

The stratified, oscillatory boundary flow over rough topography exhibits turbulence with spatial and temporal intermittency: Velocity and temperature fluctuations occur at different phases in the tidal cycle and at different locations, as discussed below. Additionally, unlike the flat-bottom boundary layer, turbulence occurs in layers with nonhomogeneous fluid that are detached from the thin well-mixed wall layer, enhancing the ability of turbulence to sustain diapycnal mixing.

4.1. Critical Slope

Where the slope angle is critical, there is a resonant baroclinic response. The boundary velocity increases, and the singularity associated with inviscid, linear theory is healed by viscous dissipation in the boundary layer. The boundary flow takes the form of a stratified, oscillating jet. **Figure 2*c*,*d*** presents an example where a boundary layer with intensified velocity can be seen on the flank of the obstacle whose slope is near critical.

The intensification, U/U_0, can be large; for example, it exceeds a value of 7 in the laboratory experiment of an oscillating plate by Zhang et al. (2008) with laminar flow ($Re_s \simeq 1$). When the Reynolds number is sufficiently high, exceeding approximately $Re_s \simeq 100$ in the DNS of Gayen & Sarkar (2010), there is transition to turbulence when the boundary flow reverses from downslope to upslope through zero velocity.

The warmer water that flows from above during the downslope phase of the flow decreases the background stratification sufficiently to create $N^2 < 0$. The ensuing convective instability creates turbulence and energizes an upslope surge of colder water as an internal bore, and shear production further enhances the fluctuation kinetic energy. There is observational evidence of patches of low or an inverted potential temperature gradient during upslope flow at near-critical slope associated with M2 internal tides, for example, at the northeast Atlantic continental slope (White 1994) and at the northwest Australian shelf (Bluteau et al. 2011) where the measured bottom intensification is $U/U_0 \simeq 6$. The turbulent loss increases with increasing length of the critical slope, reaching up to approximately 18% of the radiated flux in the DNS and LES of Gayen & Sarkar (2011b).

4.2. Top of a Supercritical Ridge

Figure 2*e*,*g* shows that, at low Ex (also Fr), there is intensified velocity at the top of the ridge. The downslope jet in the lee leads to shear-driven, boundary layer turbulence, which peaks at

maximum downslope flow. When the flow reverses, a transient lee wave is released and travels upward, leading to overturned isopycnals [e.g., the 2D simulations of Legg & Klymak (2008) that find lee waves]. 3D simulations show that, midway during the upslope phase, the wave steepens and breaks, and a patch of turbulent kinetic energy (TKE) builds up. With increasing tidal forcing velocity, the turbulent patches owing to wave breaking occur earlier during the upslope phase and become taller and have larger TKE. Kaena Ridge, Hawaii, is a steep, supercritical ($\epsilon \sim 4$) ridge, and recent transects with towed instruments at its southern slope by Alford et al. (2014) present observational evidence for the formation and breaking of lee waves, with overturns as large as 100 m during the upslope phase of the flow and near the ridge top.

4.3. Supercritical Slope

There are observations of turbulence at deep, supercritical slopes (Aucan et al. 2006, Van Haren et al. 2015), far away from the top of the obstacle. Aucan et al. (2006) detected O(100 m) overturns at a 2,425-m-deep bottom mooring on the south flank of Kaena Ridge, Hawaii, which was in the path of a downward wave beam. The overturns occurred when the shear was zero and a thermal front surged upslope. The LES of Gayen & Sarkar (2011a) of the boundary flow associated with an internal wave beam grazing the bottom supports the mechanism of convective instability during flow reversal from down- to upslope flow as a trigger for turbulence, and the model dissipation (peak of 4×10^{-7} W/kg and time average of 10^{-8} W/kg) is close to the observations of Aucan et al. (2006).

4.4. Wave-Wave Interaction

Broad, multiscale topography in the abyssal ocean such as the Mid-Atlantic Ridge (MAR) in the Brazil Basin is not particularly steep nor tall. Nevertheless, the dissipation and diffusivity over the rough patches in Brazil Basin are intensified with respect to the abyssal plain. Here, nonlinear wave-wave interactions (Polzin 2009) are thought to be responsible for the enhanced mixing over a depth of order 1 km and above the boundary layer that spans tens of meters. 2D simulations of model Brazil Basin topography by Nikurashin & Legg (2011) support the mechanism of wave-wave interaction, finding waves of frequency $\Omega - f$ with a vertical scale smaller than the M2 internal tide and susceptible to wave breaking. 3D simulations that resolve turbulence have not yet been performed for this problem.

4.5. Small-Scale Topography

Multiscale abyssal topography (e.g., the MAR) has substantial coverage, with small-scale roughness having a length scale that is not much larger than the tidal excursion length so that Ex is not small. When such small-scale, subkilometer hills have near-critical or supercritical slopes, there are breaking waves on the lee side and also above the roughness (**Figure 2*d*,*f*,*g*,*h***) as well as upslope-moving convectively unstable fronts of cold water in the bottom boundary layer. The laboratory-scale simulations of Jalali et al. (2014) of flow over a triangular obstacle indicate that, at $Ex = 0.4$, the turbulent patches extend vertically up to twice the obstacle height, and for even larger Ex, the turbulent patches extend horizontally away from the obstacle. Measurements at deep, small-scale roughness are scant, although Dale & Inall (2015) recently reported enhanced turbulence owing to upslope bores and breaking lee waves in a 100–200-m-thick bottom layer over subkilometer roughness features at a 49° N site at the MAR.

5. BAROCLINIC ENERGY BUDGET

Quantification of the energetics of the internal wave field is of utmost importance and can be done through the baroclinic energy equation (Kang & Fringer 2012), written for the sum of kinetic energy E_k and available potential energy (in the limit of small deviation from equilibrium) E_{APE} of the baroclinic motion, where

$$E_k = \frac{1}{2}\rho_0\left(u_{bc}^2 + v_{bc}^2 + w_{bc}^2\right), \quad E_{APE} = \frac{\rho_0}{2}N^{-2}b^2,$$

and the subscript bc denotes baroclinic. Let us consider an oscillatory tidal flow with amplitude $\mathbf{U}_0$ flowing over topography with height $h(x, y)$. The baroclinic energy equation is written below in the notation of Jalali et al. (2014):

$$\frac{\partial}{\partial t}(E_k + E_p) + \nabla_H \cdot \mathbf{F} = C - \rho_0\varepsilon_{bc} - P\,. \tag{3}$$

The quantities in Equation 3 are depth integrated, and ∇_H denotes horizontal divergence. The dominant term of the energy flux $\mathbf{F}$ is the wave energy flux $p^*\mathbf{u}_{bc}$ where p^* is the pressure deviation relative to the hydrostatic distribution, and the contribution of the advective flux $\boldsymbol{u}_{bc}(E_p + E_k)$ becomes important only when Ex approaches $O(1)$. The conversion, C, provides the energy input into the wave field and, in the linear case, is given by $C = p_s^*\mathbf{U}_0 \cdot \nabla h$, where p_s^* is the pressure at the surface of the topography (see Kang & Fringer 2012 for a more general expression for C). The term ε_{bc} represents the viscous dissipation of the baroclinic energy, and the term $-P$ represents the conversion to turbulent kinetic energy through the turbulent production term.

Let us consider the integral of Equation 3 over a domain enclosing the generation site and over a few tidal cycles. The net energy conversion (C) from the barotropic tide (a) is dissipated by viscosity (ε_{bc}) or converted to turbulence (P), (b) leaves the generation site as an internal wave flux (M) plus an advective flux (M_{adv}), and (c) leads to a temporal change in baroclinic energy content whose cyclic integral is close to zero if the state is close to statistically steady. The quantity $q = 1 - M/C$ measures the local energy loss, which, by construction, is zero in inviscid linear theory. DNS/LES results, albeit at laboratory scale, can be used to calculate all the terms in Equation 3, balance the budget with near-zero residual, and accurately obtain q. Results obtained thus far show that q increases with increasing values of Ex, Re, fractional length of critical slope, and bottom steepness, reaching values up to 0.3. Observations and 2D models have also been used to infer the value of q. The Hawaiian Ridge is less dissipative with $q \sim 0.15$ (Klymak et al. 2006) compared to the double-ridge Luzon Strait, which has more energetic internal tides and $q \sim 0.4$ (Alford et al. 2015). However, the quantitative accuracy of the Luzon and Hawaii estimates is uncertain, and q needs sharpening through numerical modeling.

The terms in Equation 3 are needed by ocean models that typically do not resolve internal tides. C sets the wave component of deep-ocean bottom drag in barotropic tidal models. Global climate models need C and q to set the energy input to local turbulent fluxes of buoyancy and momentum. M, the energy transported by internal waves that can propagate hundreds of kilometers, is an input for remote mixing. Thus, C, q, and M need parameterization in ocean models. For instance, St. Laurent et al. (2002) utilized dissipation measurements at the MAR and energy flux from linear theory to find $q = 0.3 \pm 0.1$ and turbulence distributed exponentially with a characteristic vertical length, 500 m. This recipe and a prescribed mixing efficiency Γ give the turbulent diffusivity. Klymak et al. (2010) proposed a parameterization of q for supercritical obstacles assuming linear theory for conversion and that high modes with phase speeds less than the ridge-top velocity amplitude are dissipated locally. It is clear from observations and simulations that the local dissipation strongly depends on topographic size, shape, and environmental parameters. Moreover, the vertical distribution of tidally driven turbulence, both local (Saenko & Merryfield

2005, Melet et al. 2013) and remote (Oka & Niwa 2013, Melet et al. 2016), strongly influences the meridional overturning circulation. Therefore, improved physically based parameterizations of dissipation and mixing are imperative.

Mixing in a stratified environment pumps buoyancy against a gravitational potential gradient. This requires an energy input, and we can relate the mixing efficiency to the fraction of energy added to the system that irreversibly raises its center of mass. The efficiency is best defined in terms of the ratio of dissipation of available potential energy to the dissipation of total (available plus kinetic) energy (for a review of the relevant concepts, see Scotti & White 2014, and references therein). In oceanographic practice it is common to define the mixing efficiency (Γ) as $\Gamma = B/\varepsilon$, where B is the buoyancy flux and ε is the turbulent dissipation. The flux Richardson number (Ri_f) is defined as $Ri_f = B/P$, where P is the shear production of TKE, and Γ is related to Ri_f as follows:

$$\Gamma = \frac{Ri_f}{1 - Ri_f}. \tag{4}$$

Following Osborn (1980), it has been common practice to set $Ri_f = 1/6$. This allows the estimation of the amount of mixing from estimates of the turbulent dissipation rate ϵ, which is easier to measure than either turbulent buoyancy fluxes or the available potential energy dissipation rate. Relating efficiency to the Richardson flux number by Equation 4 has been widely criticized in the recent literature (see Ivey et al. 2008, and references therein) because the equality is valid for stationary processes in which production of TKE is balanced locally by dissipation and turbulent buoyancy fluxes. In particular, this implies that the flow of energy is from the mean kinetic energy into the turbulent available potential energy and TKE reservoirs. This condition is realized in shear-driven mixing, but not in mixing driven by large-scale statically unstable flow arrangements. In the latter case, the turbulent buoyancy flux switches sign, signaling a transfer of mean available potential energy to TKE. Under these conditions, the mixing efficiency can be larger than 50% (Dalziel et al. 2008, Chalamalla & Sarkar 2015). Conversely, efficiencies much lower than the canonical value have been measured in stratified boundary layers (Walter et al. 2014).

The picture that emerges is that over complex terrain, different paths to turbulence and mixing are present, often at the same time, but in different parts of the domain. Close to material boundaries, the no-slip condition generates turbulent boundary layers; away from boundaries, it is often found that large-scale overturns, regions of statically unstable buoyancy distribution with little or no shear, develop (Chalamalla & Sarkar 2015). Perhaps the most interesting conclusion from these simulations is that the standard mixing paradigm à la Osborn (1980), which is based on turbulence and mixing deriving their energy from the mean kinetic energy field via the shear-production mechanism, is not always appropriate. The alternative mechanism, based on the conversion of available potential energy contained in the large-scale field into TKE via convective instabilities, needs to receive more attention. Finally, both mechanisms can be present. Gayen & Sarkar (2014) showed mixing starts as convective driven and only at a later time becomes sustained by shear.

6. PROPAGATION

Internal waves can leave the generation area either as narrow beams or as modal waves, which represent collective excitation of the entire water column, the most common being mode-1 and mode-2 waves. The case of Luzon Strait discussed above provides an illuminating example as to the form taken by the internal wave field. In the area between the east and west ridges, beams dominate, whereas in the far field on either side of the strait the internal tides acquire a mode-1 structure (Li & Farmer 2011) propagating long distances without significant attenuation (Zhao 2014). Given our emphasis on processes leading to turbulence, we focus on the evolution

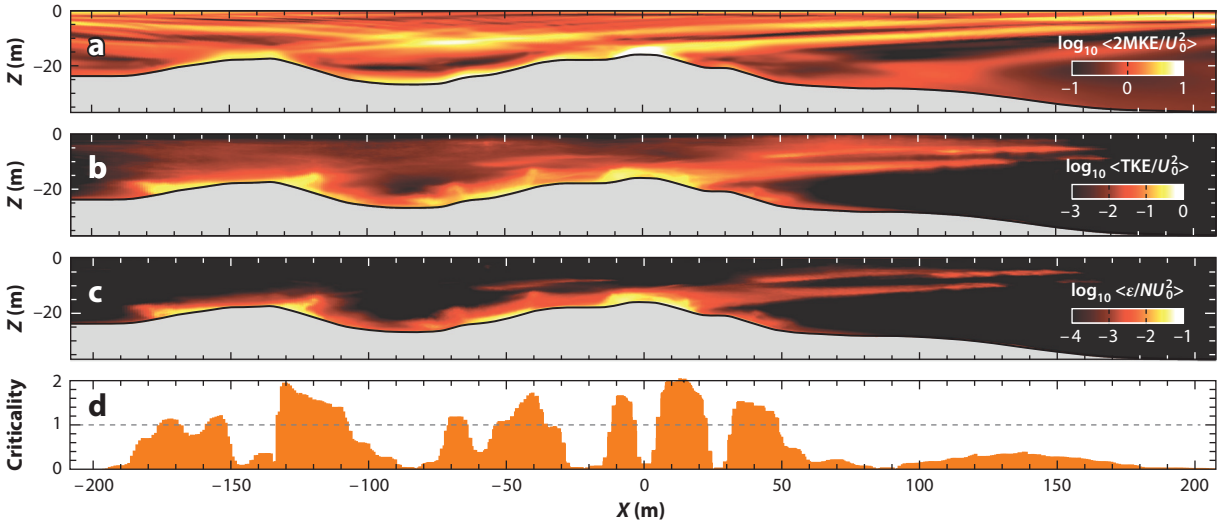

Figure 4

Flow and turbulence at a transect of the Luzon west ridge illustrated with cycle-averaged quantities: (*a*) mean kinetic energy (MKE), (*b*) turbulent kinetic energy (TKE), (*c*) turbulent dissipation rate (ε), and (*d*) local slope criticality. Quantities are normalized with the barotropic tidal amplitude U_0 and the buoyancy frequency N at the top of the ridge at $x = 0$. Turbulent dissipation, shown in panel *c*, is enhanced near the top of the supercritical subridges, at the near-critical slope (between $x = -45$ and -55 m), and at a supercritical slope (between $x = 35$ and 50 m) owing to processes discussed in Section 4. Dissipation is also enhanced during the propagation of internal wave beams owing to the processes discussed in Section 6. The large-eddy simulation (LES) uses realistic bathymetry that is scaled down 1:100 in both directions, preserving the original aspect ratio, and environmental parameters that are scaled up to preserve the values of important nondimensional parameters defined in **Table 1**, except Re, which is smaller in the LES.

of wave beams during propagation and consider low-mode waves briefly. **Figure 4** shows that, at realistic multiscale topography, turbulent processes are important at generation and in the regions where the beams propagate.

6.1. Beam-Pycnocline Interaction

If the water column is uniformly stratified all the way to the surface, beams reflect just like ordinary waves. A slow variation in stratification causes a beam to bend and refract, an effect that can be considered within the framework of WKB theory. However, when a pycnocline separates the surface layer from the more weakly stratified interior layer, the change in stratification occurs on a scale that can be short relative to the typical vertical size of beams at tidal frequencies. In this case, the reflection of beams is associated with a host of nonlinear effects that can lead to turbulence. In the case of a thin pycnocline, ISWs with large interfacial displacement have been observed (New et al. 2013), and the process has been characterized using theory and simulation (e.g., Gerkema 2001, Grisouard et al. 2011, Mercier et al. 2012). Numerical simulations of beams refracting through a pycnocline (Gayen & Sarkar 2013, Diamessis et al. 2014) show that higher harmonics can be trapped within the pycnocline and propagate. Diamessis et al. (2014) found that refraction through a thin pycnocline of a wave beam with frequency ω, wave number k, and beam angle greater than 30° relative to the horizontal plane led to the trapped harmonic $(2\omega, 2k)$ propagating as an interfacial wave. They applied weakly nonlinear theory to the analogous plane wave case with some success in the prediction of the harmonic amplitude in the simulations. However, being 2D simulations, these studies could not directly address the role of turbulence.

Gayen & Sarkar (2013) found within 2D simulations that, when the pycnocline thickness is not small compared to the vertical thickness of the incident beam, parametric subharmonic instability (PSI) occurs as the incident beam refracts through the pycnocline. Given that the vertical components of $\mathbf{k_1}$ and $\mathbf{k_2}$ can be an order of magnitude larger than that of $\mathbf{k}$, PSI is effective in cascading wave energy toward turbulence. In later 3D LES, Gayen & Sarkar (2014) demonstrated the cascade to turbulence of the subharmonic. Only 30% of the incident wave energy is contained in the main reflected beam, with the remaining carried by subharmonics from PSI (20%), ISWs and harmonics trapped in the pycnocline (15%), and other downgoing waves (35%). That only 30% of the incoming energy is carried away by the reflected beam may explain why energetic beams are typically confined near the source region (e.g., at Kaena Ridge) (Cole et al. 2009). The mixing efficiency of the ensuing turbulence was approximately 0.3, almost twice the canonical value. This may result from turbulence being initially driven by overturns, and later sustained by shear.

Parametric subharmonic instability (PSI): instability that transfers energy from a wave of frequency Ω and wave vector $\mathbf{k}$ to two waves of lower frequency, such that $\mathbf{k} = \mathbf{k_1} + \mathbf{k_2}$ and $\Omega = \Omega_1 + \Omega_2$

Critical layer: region where the local background velocity matches the phase velocity of the wave and the Doppler-shifted frequency approaches zero

6.2. Beam-Beam Interaction

When two beams emanating from different locales interact, the superposition can lead to nonlinear phenomena, including higher harmonics (Akylas & Karimi 2012). The effect can be particularly important when the beams originate from different points along a single 3D topographic feature. The common origin means that phases and frequencies along the intersecting beams are correlated, providing an example of wave focusing (Bühler & Muller 2007). Experiments with purely inertial wave beams (Duran-Matute et al. 2013) show that the focusing can lead to sustained levels of turbulence. More research is needed to determine how much energy can be lost via beam-beam interaction, and how efficient the process is in the stratified case.

6.3. Within-Beam Turbulence

The beams that emerge from rough topography can be strongly nonlinear if they are sufficiently energetic so that $Fr_w \sim O(1)$ and, when Ri becomes sufficiently small, there is turbulence (Jalali et al. 2014). The presence of internal wave beams that emerge from the two flanks of Kaena Ridge is clear in the velocity variance observed by Cole et al. (2009), and the inferred turbulent dissipation is found to be large in the region bounded by the beams as they propagate toward the upper ocean pycnocline. PSI can also result in the instability of freely propagating beams, as shown experimentally by Bourget et al. (2014) and analytically by Karimi & Akylas (2014), who demonstrated that the beam must be sufficiently wide and Fr_w must be sufficiently large for PSI to occur.

6.4. Critical Layer

Internal waves can also interact with shear layers to generate turbulence at so-called critical layers. This mechanism has been widely studied using theory and laboratory experiments, and observationally in the atmospheric context, but less so in the ocean. Waterman et al. (2012) presented evidence that this occurs for both near-inertial waves propagating downward and internal (lee) waves propagating upward in the Antarctic Circumpolar Current.

6.5. Low-Mode Wave

The energy flux of the internal tides in the far field of ridges has a low-mode structure, primarily modes 1 and 2, with large horizontal wavelength. The low mode interacts with currents, eddies,

and fronts during propagation that may cascade energy to smaller vertical scales. However, direct evidence of such a cascade is scant.

PSI can transfer energy to high vertical modes and can be especially potent for the M2 tide at the critical latitude (28.9°) when the M2/2 subharmonic frequency exactly matches f, as shown numerically by MacKinnon & Winters (2005). Alford et al. (2007) observed intense, vertically standing, near-inertial waves near 28.9° that suggest PSI, but with no significant loss in the M2 tidal energy flux, and consistent with these observations, the numerical simulations of Hazewinkel & Winters (2011) find the energy transfer through PSI to be small. Later analysis of these observations by MacKinnon et al. (2013) revealed PSI-consistent energy transfer at 28.9° N, but it did not lead to a catastrophic decay of the M2 tide.

Superharmonics with 2ω and $2k$ found in the refraction of an internal wave beam can also occur through the nonlinear self-interaction of a low-mode wave that propagates in nonuniform stratification. Wunsch (2015) examined this process using weakly nonlinear theory to evaluate the steady-state amplitude of the superharmonic as a function of upper-ocean pycnocline properties. Sutherland (2016) evaluated the unsteady evolution of the problem using numerical simulation and noted the appearance of vertical scales in the superharmonic that are smaller than in the primary wave.

Scattering off topography in the mid-ocean and reflection at the rough continental slope are likely to be the important sinks for the low-mode energy. Reflection is surveyed in the following section. The problem of scattering of waves by roughness has been treated using theory or simulation by Bühler & Holmes-Cerfon (2011), Legg (2014), and Mathur et al. (2014). Scattering may involve local energy dissipation or a shift of transmitted and reflected wave energy to higher modes. Bühler & Holmes-Cerfon (2011) showed analytically that wave energy can be focused into high modes with beam-like character as a mode-1 wave propagates over a rough bottom with continuous subcritical topography. The energy loss from the mode-1 wave with wave number k was shown to be substantial after approximately $O(10)$ surface bounces of the wave characteristic for sinusoidal topography that is a harmonic of the incoming wave or for random topography. From the simulations of Legg (2014), it appears that significant turbulent loss during scattering at isolated mid-ocean roughness requires tall features and/or near-critical slopes. Accurate quantification of the turbulence and attendant mixing by scattering of low-mode wave energy will require 3D, turbulence-resolving simulations.

7. REFLECTION AT SLOPING TOPOGRAPHY

A substantial portion of the energy generated at generation hotspots escapes as low-mode internal tides and is able to propagate to the continental slope. Interaction of internal tides with rough topography can generate fine-scale shear and strain, as well as boundary layer turbulence. The following discussion of internal wave reflection excludes ISWs, comprehensively reviewed by Lamb (2014).

7.1. Theory for Beams Incident upon Slopes

According to linear theory, the angle of phase lines (equivalently, the group velocity) with respect to the horizontal plane is preserved after the reflection of an internal wave beam. The wave number decreases as the wave angle (α) approaches the slope angle (β), and within inviscid theory, the wave speed increases to preserve wave energy flux. Theory in frequency space shows that for a wave with incident $Fr_\mathrm{i} = U/c_\mathrm{p} = uk/\omega$, the Froude number of the reflected wave satisfies

$$\frac{Fr_\mathrm{r}}{Fr_\mathrm{i}} = \left[\frac{\sin(\alpha+\beta)}{\sin(\alpha-\beta)}\right]^2. \quad (5)$$

The singularity at critical slope angle ($\alpha = \beta$) is usually resolved by the inclusion of viscosity or nonlinearity. Analysis in the time domain (Dauxois & Young 1999, Scotti 2011) allows the construction of a laminar inviscid solution even at criticality and thus the examination of possible pathways to turbulence. For example, Scotti (2011) found both convective and shear instability. Exact criticality is not necessary for nonlinear processes. When the off-criticality ($\alpha - \beta$) is small, the amplification of Fr is large: by a factor of 100 (10) when the slope off-criticality is approximately 18% (48%) of the wave angle according to Equation 5, where we have replaced sin(·) by its argument. Thus, the reflected wave can have $Fr = O(1)$ even though the incident wave has small steepness, begetting nonlinear phenomena including harmonics, PSI, and wave breaking. The Richardson number, $Ri = N^2/S^2$, proportional to Fr^{-2}, strongly decreases when $\alpha - \beta$ is small to facilitate shear instability.

The incident and reflected waves interact. Even though both waves may be linear, the inclusion of nonlinearity in the interaction can lead to propagating harmonics and a mean Eulerian current. It is possible for the forced harmonic (2Ω or higher) to interact resonantly with the incident and reflected waves, and the second-order or higher interactions to steepen the waves in the interaction region (Thorpe 1987).

7.2. Observations

Eriksen (1982) analyzed near-bottom data from several sites with rough topography, finding intensified spectral levels at the local near-critical band of frequencies, $Ri_g \sim 0.25$ at vertical separations up to 40 m, and well-mixed patches. Thorpe et al. (1990) observed O(100 m) isopycnal displacements and transient mixed layers with M2 variability at two sites on the continental slope of Ireland and associated them with critical-slope reflection and resonant second-order reflection. Reflection of low-mode internal wave energy at near-critical slopes has been implicated in observations of enhanced M2 band shear and turbulent dissipation at a steep continental slope off Virginia (Nash et al. 2004), and also at the Oregon continental slope (Nash et al. 2007) with hotspots of dissipation, $\varepsilon > 10^{-7}$ W/kg. Near-critical generation could also play a part at the Oregon slope.

The recent Tasmanian Tidal Dissipation Experiment (T-TIDE) examines the fate of a coherent low-mode internal wave that is incident on the continental slope off Tasmania, an area that has specific sites with a preponderance of either supercritical or near-critical topography. The objective is to measure how much of the incoming wave energy is dissipated locally and to quantify the downscale cascade of incident wave energy. As summarized by Pinkel et al. (2015), a suite of shipboard observations, gliders, and deep moorings is being used along with numerical modeling.

The mixed fluid in the boundary layer at continental slope roughness could spread across isopycnals to provide interior mixing, as first proposed by Armi (1978). Intermediate nepheloid layers observed near continental margins (Moum et al. 2002, McPhee-Shaw 2006) lend some support to this hypothesis. Although mixed fluid can propagate away from the slope, initially propelled by its buoyancy anomaly and then mesoscale processes, it is not clear how far can it propagate. Intermediate nepheloid layers are usually found extending only O(10 km) from the margins. However, this may be a limitation of the tracer used to map them (usually suspended sediments). Irrespective of where the mixed fluid associated with rough topography forms, in the bottom boundary layer or by wave breaking further away in the bottom water column, its horizontal spread needs further investigation.

7.3. Laboratory Experiments

The reflection of high-mode internal wave beams has been the subject of several experimental studies, which have showed that turbulence during the reflection process can occur both attached

to the wall and in regions detached from the boundary (De Silva et al. 1997). In the past decade or so, there have been exciting developments in experimental techniques. Gostiaux et al. (2006) used a beam generator, later perfected by Gostiaux et al. (2007), to investigate how beams reflect from sloping boundaries. These generators enable beams with tunable properties and have been used to study the formation of harmonics during reflection (Rodenborn et al. 2011). New techniques have also been developed to extract quantitative information from experiments, e.g., the use of synthetic schlieren imaging (Peacock & Tabaei 2005) or planar laser-induced fluorescence (Troy & Koseff 2005).

Whereas reflecting finite-width beams affect only a small area along the slope, low-mode waves in a uniformly stratified fluid interact with the entire slope. The interaction region in the case of a low-mode wave incident on a linear slope with critical angle takes the form of a turbulent boundary layer over the entire slope, as first shown experimentally by Ivey & Nokes (1989), who found turbulence if the wave Reynolds number exceeded a critical value of 15–20. A background with two-layer stratification supports the horizontal propagation of interfacial sinusoidal waves as well as internal solitary waves. Lamb (2014) reviewed the breaking of such horizontally propagating waves as they shoal onto a slope and pointed out essential differences with the uniformly stratified case.

7.4. Numerical Simulations

The interaction of a plane wave with a linear slope in a uniformly stratified fluid has been studied using 3D simulations at the laboratory scale. Chalamalla et al. (2013) assessed the effect of incoming wave properties through 3D DNS, expanding on the earlier work of Slinn & Riley (1998) on critical slopes. The reflected wave Fr_r increases with the incoming wave amplitude in accord with Equation 5: Multiple harmonics are radiated, and the boundary layer transitions to turbulence when $Fr_\mathrm{r} \simeq 0.3$. Interestingly, off-critical slopes also exhibit turbulence when $\alpha - \beta$ is not too large. In fact, because of weaker frictional effects and the stronger interaction between the incident and reflected waves, some off-critical slopes were found to exhibit taller overturns and larger TKE than the critical slope at the same Fr. For the same off-criticality, the supercritical slope has stronger turbulence than the subcritical slope because of larger Fr_r, and may have turbulence that exceeds that at a critical slope if the off-critical angle is not too large.

In the case of wave beams, the reflected wave can undergo PSI under off-critical conditions owing to an increase of Fr, as demonstrated through 2D simulations by Chalamalla & Sarkar (2016). Higher-amplitude and wider incoming beams result in reflected waves with enhanced subharmonic growth rate, similar to freely propagating beams considered by Bourget et al. (2014) and Karimi & Akylas (2014), and there is a threshold for Fr_r before the onset of PSI. The potential cascade of subharmonics of the reflected beam to turbulence remains to be assessed.

Venayagamoorthy & Fringer (2006) studied the energetics of the interaction of mode-1 waves with a shelf break at the laboratory scale using 2D simulations. They found that reflection is negligible for a shallow slope ($\gamma < 0.75$) and is large for a steep, supercritical slope. Increasing the incoming Fr_i and slope angle resulted in the formation of boluses but did not change the energy transmission much for critical slopes and beyond because the boluses provide bursts of energy onto the shelf. The dynamics of the nonlinear internal boluses that carry dense, cold water on shelf were further examined by Venayagamoorthy & Fringer (2007), who found that the boluses have properties consistent with gravity currents propagating in a stratified fluid. Recently, Winters (2015) examined the interaction of a mode-1 wave with a supercritical slope ($\gamma = 1.9$) using high-resolution, 3D simulations. The Reynolds number, $Re = U_0^2/N\nu = 5.5 \times 10^4$, is large, and the incident wave has $Fr_\mathrm{i} = 0.128$. Although off-critical, there is turbulence associated with quasi-periodic bores, which enhances the effective diffusivity of synthetic tracer released at the boundary.

8. NONTIDAL TURBULENCE AT TOPOGRAPHY

Motions of nontidal origin such as currents, mesoscale eddies, and fronts can impinge on rough topography in the deep ocean to generate internal waves whose local and remote breaking can lead to turbulent mixing, e.g., in the Southern Ocean where such nontidal motions are strong and deep, extending to the seafloor. Naveira Garabato et al. (2004) observed widespread (order of 1,000-km horizontal distance) enhancement of internal wave fluctuations over rough bathymetry underneath the Antarctic Circumpolar Current, which was attributed in part to nontidal, geostrophic motions. Nikurashin & Ferrari (2010) found that radiated internal waves interact with the shear of near-inertial oscillations, leading to wave breaking in their 2D simulations. Wind-driven geostrophic flow develops energetic meso- and submesoscale motions that can interact with rough topography. Using nonhydrostatic simulations with the MITgcm, Nikurashin et al. (2013) found that a dominant fraction of the wind power was converted from geostrophic eddies to small-scale motions, which, within the bottom 100 m over the seafloor, led to most of the diagnosed dissipation.

Strong overflows can provide turbulent mixing (Thurnherr et al. 2005, St. Laurent & Thurnherr 2007) at major deep ocean passages as well as smaller passages that are typical in the rough topography of mid-ocean ridges. Observations by St. Laurent & Thurnherr (2007) at such a passage near the crest of the MAR in the subtropical Atlantic Ocean indicate large turbulent diffusivities near the bottom, which remain significant up to the base of the main thermocline. The measured Froude number supports the notion of hydraulic control at a sill with a possible downstream hydraulic jump in the passage.

9. CONCLUSIONS AND FUTURE DIRECTIONS

The large-scale mechanical forcing of the world oceans takes primarily two forms: lunisolar tides and wind forcing at the surface. Understanding how this energy reaches, in the stratified ocean interior, the small scales at which turbulence and mixing occur has been a long-standing question in physical oceanography. The amount of tidal energy that is not dissipated over shallow seas energizes internal waves by interaction with topography, and this review considers recent advances in understanding the interplay of internal waves and turbulence over the cycle of internal wave generation, propagation, and reflection.

The field has benefited tremendously from a series of large coordinated experiments over the past decade, involving field measurements, numerical models, and theoretical work, starting with HOME, followed by IWISE, and continuing with the recently concluded T-TIDE, which have been made possible by a combination of better observational platforms and instrumentation, better regional ocean models and process models run on more powerful computers, and better remote-sensing tools.

We are now in a position to satisfactorily answer questions related to how the energy injected at the generation site is split between energy lost locally to turbulence and energy that radiates away as a function of the parameters that describe the geometry of the topography and the nonlinearity of the process. Similarly, we can address similar questions for the reflection process although we are not as far along toward the answers. At the same time, the high-resolution numerical models are challenging some long-held assumptions regarding the mixing efficiency of different turbulent processes.

Although these findings help us understand how turbulence generated during generation and reflection influences mixing in the proximity of boundaries, the way internal waves propagating in the water column affect mixing remains more obscure. Over complex topography, nonlinearity and turbulence can be generated by the interaction of beams coming from multiple generation sites, but internal waves can also interact with critical layers, or with a region of strongly varying

background stratification. Most modeling work in this area has been 2D (with exceptions) and thus not able to directly address the role of turbulence.

Looking at the future, we see great potential in modeling frameworks that can span increasingly broader ranges of spatial and temporal scales as well as 3D topography while accounting for instabilities and turbulent processes through a combination of nested, high-resolution subdomains and physics-based parameterizations. However, we must recognize the role of observations in providing a grounding truth, as well as the role of theoretical frameworks to pose the right questions and extract the right answers out of ever expanding numerical and observational data sets.

SUMMARY POINTS

1. The nature of the internal waves generated by an oscillating tidal flow over topography depends on the steepness, excursion number, and topographic Froude number. At low excursion numbers, high-mode beams are generated. As excursion numbers approach $O(1)$, lee waves are more common. Near-critical slopes have intensified boundary flows. At low Froude numbers, there is flow blocking, and for steep supercritical topography, there are downslope jets and breaking lee waves.
2. Internal wave beams are more commonly found near the generation region, whereas farther away low-mode waves dominate.
3. Proper simulation of turbulent processes requires 3D domains and resolution of convective and shear instability. With LES, it is possible to access the turbulence produced by waves generated by quasi-2D topography.
4. Patches of turbulence are more commonly associated with high-mode internal wave beams and lee waves than with low-mode waves.
5. Wave-wave interactions, resonances, and intersecting beams from multiple features promote turbulence at sites with multiscale topography.
6. Nontidal topographic internal waves can contribute significantly to turbulence and mixing in the Antarctic Circumpolar Current system.

DISCLOSURE STATEMENT

The authors are not aware of any biases that might be perceived as affecting the objectivity of this review.

ACKNOWLEDGMENTS

S.S. was supported by NSF grant OCE-1459774 and ONR grant N00014-15-1-2578. A.S. was supported by NSF grant OCE-1459506 and ONR grant N00014-15-1-2578. S.S. acknowledges the contributions of B. Gayen, V. Chalamalla, M. Jalali, and N. Rapaka to his research on this topic.

LITERATURE CITED

Akylas T, Karimi H. 2012. Oblique collisions of internal wave beams and associated resonances. *J. Fluid Mech.* 711:337–63

Alford MH, Klymak JM, Carter GS. 2014. Breaking internal lee waves at Kaena Ridge, Hawaii. *Geophys. Res. Lett.* 41:906–12

Alford MH, MacKinnon JA, Zhao Z, Pinkel R, Klymak J, Peacock T. 2007. Internal waves across the Pacific. *Geophys. Res. Lett.* 34:L24601

Alford MH, Peacock T, MacKinnon JA, Nash JD, Buijsman MC, et al. 2015. The formation and fate of internal waves in the South China Sea. *Nature* 521:65–69

Armi L. 1978. Some evidence for boundary mixing in the deep ocean. *J. Geophys. Res.* 83:1971–79

Arnold VI, Khesin BA. 1998. *Topological Methods in Hydrodynamics*. New York: Springer

Aucan J, Merrifield MA, Luther DS, Flament P. 2006. Tidal mixing events on the deep flanks of Kaena Ridge, Hawaii. *J. Phys. Oceanogr.* 36:1202–19

Baines PG. 1995. *Topographic Effects in Stratified Flows*. Cambridge, UK: Cambridge Univ. Press

Becker JJ, Sandwell DT. 2008. Global estimates of seafloor slope from single-beam ship soundings. *J. Geophys. Res. Oceans* 113:C05028

Bell TH. 1975. Lee waves in stratified fluid with simple harmonic time dependence. *J. Fluid Mech.* 67:705–22

Blayo E, Debreu L. 2006. Nesting ocean models. In *Ocean Weather Forecasting*, ed. EP Chassignet, J Verron, pp. 127–46. New York: Springer

Bluteau CE, Jones NL, Ivey GN. 2011. Dynamics of a tidally forced stratified shear flow on the continental slope. *J. Geophys. Res.* 116:C11017

Bourget B, Scolan H, Dauxois T, Le Bars M, Odier P, Joubaud S. 2014. Finite-size effects in parametric subharmonic instability. *J. Fluid Mech.* 759:739–50

Bühler O, Holmes-Cerfon M. 2011. Decay of an internal tide due to random topography in the ocean. *J. Fluid Mech.* 678:271–93

Bühler O, Muller CJ. 2007. Instability and focusing of internal tides in the deep ocean. *J. Fluid Mech.* 588:1–28

Buijsman M, Klymak JM, Legg S, Alford MH, Farmer D, et al. 2013. Three-dimensional double-ridge internal tide resonance in Luzon Strait. *J. Phys. Oceanogr.* 44:850–69

Buijsman M, Legg S, Klymak J. 2012. Double ridge internal tide interference and its effect on dissipation in Luzon Strait. *J. Phys. Oceanogr.* 42:1337–56

Cacchione DA, Pratson LF, Ogston AS. 2002. The shaping of continental slopes by internal tides. *Science* 296:724–27

Carter GS, Gregg MC. 2002. Intense, variable mixing near the head of Monterey Submarine Canyon. *J. Phys. Oceanogr.* 32:3145–65

Chalamalla VK, Gayen B, Scotti A, Sarkar S. 2013. Turbulence during the reflection of internal gravity waves at critical and near-critical slopes. *J. Fluid Mech.* 729:47–68

Chalamalla VK, Sarkar S. 2015. Mixing, dissipation rate, and their overturn-based estimates in a near-bottom turbulent flow driven by internal tides. *J. Phys. Oceanogr.* 45:1969–87

Chalamalla VK, Sarkar S. 2016. PSI in the case of internal wave beam reflection at a uniform slope. *J. Fluid Mech.* 789:347–67

Cole ST, Rudnick DL, Hodges BA, Martin JP. 2009. Observations of tidal internal wave beams at Kauai channel, Hawaii. *J. Phys. Oceanogr.* 39:421–36

Dale AC, Inall ME. 2015. Tidal mixing processes amid small-scale deep-ocean topography. *Geophys. Res. Lett.* 42:484–91

Dalziel SB, Patterson MD, Caulfield CP, Coomaraswamy IA. 2008. Mixing efficiency in high-aspect-ratio Rayleigh-Taylor experiments. *Phys. Fluids* 20:065106

Dauxois T, Young WR. 1999. Near-critical reflection of internal waves. *J. Fluid Mech.* 390:271–95

De Silva IPD, Imberger J, Ivey GN. 1997. Localized mixing due to a breaking internal wave ray at a sloping bed. *J. Fluid Mech.* 350:1–27

Debreu L, Marchesiello P, Penven P, Cambon G. 2012. Two-way nesting in split-explicit ocean models: algorithms, implementation and validation. *Ocean Model.* 49:1–21

Diamessis P, Wunsch S, Delwiche I, Richter M. 2014. Nonlinear generation of harmonics through the interaction of an internal wave beam with a model oceanic pycnocline. *Dyn. Atmos. Oceans* 66:110–37

Duran-Matute M, Flór JB, Godeferd FS, Jause-Labert C. 2013. Turbulence and columnar vortex formation through inertial-wave focusing. *Phys. Rev. E* 87:041001

Echeverri P, Flynn MR, Winters KB, Peacock T. 2009. Low-mode internal tide generation by topography: an experimental and numerical investigation. *J. Fluid Mech.* 636:91–108

Egbert GD, Ray RD. 2001. Estimates of M_2 tidal dissipation from TOPEX/Poseidon altimeter data. *J. Geophys. Res.* 106:22475–502
Eriksen CC. 1982. Observations of internal wave reflection off sloping bottoms. *J. Geophys. Res.* 87:525–38
Garrett C, Kunze E. 2007. Internal tide generation in the deep ocean. *Annu. Rev. Fluid Mech.* 39:57–87
Gayen B, Sarkar S. 2010. Turbulence during the generation of internal tide on a critical slope. *Phys. Rev. Lett.* 104:218502
Gayen B, Sarkar S. 2011a. Boundary mixing by density overturns in an internal tidal beam. *Geophys. Res. Lett.* 38:L14608
Gayen B, Sarkar S. 2011b. Direct and large eddy simulations of internal tide generation at a near critical slope. *J. Fluid Mech.* 681:48–79
Gayen B, Sarkar S. 2013. Degradation of an internal wave beam by parametric subharmonic instability in an upper ocean pycnocline. *J. Geophys. Res. Oceans* 118:4689–98
Gayen B, Sarkar S. 2014. PSI to turbulence during internal wave beam refraction through the upper ocean pycnocline. *Geophys. Res. Lett.* 41:8953–60
Gerkema T. 2001. Internal and interfacial tides: beam scattering and local generation of solitary waves. *J. Mar. Res.* 59:227–55
Gostiaux L, Dauxois T, Didelle H, Sommeria J, Viboud S. 2006. Quantitative laboratory observations of internal wave reflection on ascending slopes. *Phys. Fluids* 18:056602
Gostiaux L, Didelle H, Mercier S, Dauxois T. 2007. A novel internal waves generator. *Exp. Fluids* 42:123–30
Grisouard N, Staquet C, Gerkema T. 2011. Generation of internal solitary waves in a pycnocline by an internal wave beam: a numerical study. *J. Fluid Mech.* 676:491–513
Hazewinkel J, Winters KB. 2011. PSI of the internal tide on a β plane: flux divergence and near-inertial wave propagation. *J. Phys. Oceanogr.* 41:1673–82
Ivey GN, Nokes RI. 1989. Vertical mixing due to the breaking of critical internal waves on sloping boundaries. *J. Fluid Mech.* 204:479–500
Ivey GN, Winters KB, Koseff JR. 2008. Density stratification, turbulence, but how much mixing? *Annu. Rev. Fluid Mech.* 40:169–84
Jalali M, Chalamalla VK, Sarkar S. 2016. On the accuracy of overturn-based estimates of turbulent dissipation at rough topography. *J. Phys. Oceanogr.* Submitted manuscript
Jalali M, Rapaka N, Sarkar S. 2014. Tidal flow over topography: effect of excursion number on wave energetics and turbulence. *J. Fluid Mech.* 750:259–83
Jayne SR. 2009. The impact of abyssal mixing parameterizations in an ocean general circulation model. *J. Phys. Oceanogr.* 39:1756–75
Kang D, Fringer O. 2012. Energetics of barotropic and baroclinic tides in the Monterey Bay area. *J. Phys. Oceanogr.* 42:272–90
Karimi HH, Akylas TR. 2014. Parametric subharmonic instability of internal waves: locally confined beams versus monochromatic wavetrains. *J. Fluid Mech.* 757:381–402
Klymak JM, Legg S, Pinkel R. 2010. A simple parameterization of turbulent tidal mixing near supercritical topography. *J. Phys. Oceanogr.* 40:2059–74
Klymak JM, Moum JN, Nash JD, Kunze E, Girton JB, et al. 2006. An estimate of tidal energy lost to turbulence at the Hawaiian Ridge. *J. Phys. Oceanogr.* 36:1148–64
Korobov AS, Lamb KG. 2008. Interharmonics in internal gravity waves generated by tide-topography interaction. *J. Fluid Mech.* 611:61–95
Kunze E, Toole JM. 1997. Tidally driven vorticity, diurnal shear and turbulence atop Fieberling Seamount. *J. Phys. Oceanogr.* 27:2663–93
Lamb KG. 2004. Nonlinear interaction among internal wave beams generated by tidal flow over supercritical topography. *Geophys. Res. Lett.* 31:L09313
Lamb KG. 2014. Internal wave breaking and dissipation mechanisms on the continental slope/shelf. *Annu. Rev. Fluid Mech.* 46:231–54
Legg S. 2014. Scattering of low-mode internal waves at finite isolated topography. *J. Phys. Oceanogr.* 44:359–83
Legg S, Klymak J. 2008. Internal hydraulic jumps and overturning generated by tidal flows over a tall steep ridge. *J. Phys. Oceanogr.* 38:1949–64

Leichter JJ, Stewart HL, Miller SL. 2003. Episodic nutrient transport of Florida coral reefs. *Limnol. Oceanogr.* 48:1394–407
Li Q, Farmer DM. 2011. The generation and evolution of nonlinear internal waves in the deep basin of the South China Sea. *J. Phys. Oceanogr.* 41:1345–63
Llewellyn Smith SG, Young WR. 2002. Conversion of the barotropic tide. *J. Phys. Oceanogr.* 32:1554–66
Lueck RG, Mudge TD. 1997. Topographically induced mixing around a shallow seamount. *Science* 276:1831–33
MacKinnon JA, Alford MH, Sun O, Pinkel R, Zhao Z, Klymak J. 2013. Parametric subharmonic instability of the internal tide at 29°N. *J. Phys. Oceanogr.* 43:17–28
MacKinnon JA, Winters KB. 2005. Subtropical catastrophe: significant loss of low-mode tidal energy at 28.9°. *Geophys. Res. Lett.* 32:L15605
Mathur M, Carter GS, Peacock T. 2014. Topographic scattering of the low-mode internal tide in the deep ocean. *J. Geophys. Res.* 119:2165–82
McPhee-Shaw EE. 2006. Boundary-interior exchange: reviewing the idea that internal-wave mixing enhances lateral dispersal near continental margins. *Deep-Sea Res.* 43:42–59
Melet A, Hallberg R, Legg S, Polzin K. 2013. Sensitivity of the ocean state to the vertical distribution of internal-tide-driven mixing. *J. Phys. Oceanogr.* 43:602–15
Melet A, Legg S, Hallberg R. 2016. Climatic impacts of parameterized local and remote tidal mixing. *J. Climate* 29:3473–500
Menemenlis D, Campin JM, Heimbach P, Hill C, Lee T, et al. 2008. ECCO2: high resolution global ocean and sea ice data synthesis. *Mercator Ocean Q. Newsl.* 31:13–21
Mercier MJ, Mathur M, Gostiaux L, Gerkema T, Magalhães, et al. 2012. Soliton generation by internal tidal beams impinging on a pycnocline: laboratory experiments. *J. Fluid Mech.* 704:37–60
Moum JN, Caldwell DR, Nash JD, Gunderson GD. 2002. Observations of boundary mixing over the continental slope. *J. Phys. Oceanogr.* 32:2113–30
Munk W, Wunsch C. 1998. Abyssal recipes II: energetics of tidal and wind mixing. *Deep-Sea Res. I* 45:1977–2010
Nash JD, Alford MH, Kunze E, Martini K, Kelly S. 2007. Hotspots of deep ocean mixing on the Oregon continental slope. *Geophys. Res. Lett.* 34:L01605
Nash JD, Kunze E, Toole JM, Schmitt RW. 2004. Internal tide reflection and turbulent mixing on the continental slope. *J. Phys. Oceanogr.* 34:1117–34
Naveira Garabato A, Polzin K, King B, Heywood K, Visbeck M. 2004. Widespread intense turbulent mixing in the Southern Ocean. *Science* 303:210–13
New A, Magalhaes J, da Silva J. 2013. Internal solitary waves on the Saya de Malha bank of the Mascarene Plateau: SAR observations and interpretation. *Deep-Sea Res. I* 79:50–61
Nikurashin M, Ferrari R. 2010. Radiation and dissipation of internal waves generated by geostrophic motions impinging on small-scale topography: theory. *J. Phys. Oceanogr.* 40:1055–74
Nikurashin M, Legg S. 2011. A mechanism for local dissipation of internal tides at rough topography. *J. Phys. Oceanogr.* 41:378–95
Nikurashin M, Vallis GK, Adcroft A. 2013. Routes to energy dissipation for geostrophic flows in the Southern Ocean. *Nat. Geosci. Lett.* 6:48–51
Oka A, Niwa Y. 2013. Pacific deep circulation and ventilation controlled by mixing away from the sea bottom. *Nat. Commun.* 4:2419
Osborn T. 1980. Estimates of the local rate of vertical diffusion from dissipation measurements. *J. Phys. Oceanogr.* 10:83–89
Osborne AR, Burch TL, Scarlet RI. 1978. The influence of internal waves on deepwater drilling. *J. Petrol. Technol.* 30:1497–504
Peacock T, Tabaei A. 2005. Visualization of nonlinear effects in reflecting internal wave beams. *Phys. Fluids* 17:061702
Pétrélis F, Llewellyn Smith SG, Young WR. 2006. Tidal conversion at submarine ridge. *J. Phys. Oceanogr.* 36:1053–71
Piggott M, Gorman G, Pain C, Allison P, Candy A, et al. 2008. A new computational framework for multi-scale ocean modelling based on adapting unstructured meshes. *Int. J. Numer. Methods Fluids* 56:1003–15

Pingree RD, New AL. 1992. Downward propagation of internal tidal energy into the Bay of Biscay. *Deep-Sea Res.* 36:735–58

Pinkel R, Alford M, Lucas AJ, Johnston S, MacKinnon J, et al. 2015. Turbulent dynamics of a critically reflecting internal gravity wave. *Eos* 96. doi:10.1029/2015EO039555

Polzin K. 2009. An abyssal recipe. *Ocean Model.* 30:298–309

Polzin K, Toole JM, Ledwell JR, Schmnitt RW. 1997. Spatial variability of turbulent mixing in the abyssal ocean. *Science* 276:93–96

Rainville L, Pinkel R. 2006. Baroclinic energy flux at the Hawaiian Ridge: observations from the R/P FLIP. *J. Phys. Oceanogr.* 36:1104–22

Rapaka N, Gayen B, Sarkar S. 2013. Tidal conversion and turbulence at a model ridge: direct and large eddy simulations. *J. Fluid Mech.* 715:181–209

Rodenborn B, Kiefer D, Zhang H, Swinney HL. 2011. Harmonic generation by reflecting internal waves. *Phys. Fluids* 23:026601

Rudnick DL, Boyd TJ, Brainard RE, Carter GS, Egbert GD, et al. 2003. From tides to mixing along the Hawaiian Ridge. *Science* 301:355–57

Saenko OA. 2005. The effect of localized mixing on the ocean circulation and time-dependent climate change. *J. Phys. Oceanogr.* 36:140–60

Saenko OA, Merryfield WJ. 2005. On the effect of topographically enhanced mixing on the global ocean circulation. *J. Phys. Oceanogr.* 35:826–34

Santilli E, Scotti A. 2011. An efficient method for solving highly anisotropic elliptic equations. *J. Comput. Phys.* 230:8342–59

Santilli E, Scotti A. 2015. The stratified ocean model with adaptive refinement (SOMAR). *J. Comput. Phys.* 291:60–81

Scotti A. 2011. Inviscid critical and near-critical reflection of internal waves in the time domain. *J. Fluid Mech.* 674:464–88

Scotti A, Mitran S. 2008. An approximated method for the solution of elliptic problems in thin domains: application to nonlinear internal waves. *Ocean Model.* 25:144–53

Scotti A, White B. 2014. Diagnosing mixing in stratified turbulent flows with a locally defined available potential energy. *J. Fluid Mech.* 740:114–35

Slinn DN, Riley JJ. 1998. Turbulent dynamics of a critically reflecting internal gravity wave. *Theor. Comput. Fluid Dyn.* 11:281–303

Sobolev SL. 1955. On a new problem of mathematical physics. *Izv. USSR Akad. Sci. Mat.* 18:3–50

St. Laurent L, Simmons H, Jayne S. 2002. Estimating tidally driven mixing in the deep ocean. *Geophys. Res. Lett.* 29:2106

St. Laurent LC, Thurnherr AM. 2007. Intense mixing of lower thermocline water on the crest of the Mid-Atlantic Ridge. *Nat. Lett.* 448:680–83

Sutherland BR. 2016. Excitation of superharmonics by internal modes in non-uniformly stratified fluid. *J. Fluid Mech.* 793:335–52

Thorpe SA. 1987. On the reflection of a train of finite-amplitude internal waves from a uniform slope. *J. Fluid Mech.* 178:279–302

Thorpe SA, Hall P, White M. 1990. The variability of mixing at the continental slope. *Philos. Trans. R. Soc. Lond. A* 331:183–94

Thurnherr AM, St. Laurent LC, Speer KG, Toole JM, Ledwell JR. 2005. Mixing associated with sills in a canyon on the mid-ocean ridge flank. *J. Phys. Oceanogr.* 35:1370–81

Troy C, Koseff J. 2005. The generation and quantitative visualization of breaking internal waves. *Exp. Fluids* 38:549–62

Van Haren H, Cimatoribus A, Gostiaux L. 2015. Where large deep-ocean waves break. *Geophys. Res. Lett.* 42:2351–57

Venayagamoorthy SK, Fringer OB. 2006. Numerical simulations of the interaction of internal waves with a shelf break. *Phys. Fluids* 18:076603

Venayagamoorthy SK, Fringer OB. 2007. On the formation and propagation of nonlinear internal boluses across a shelf break. *J. Fluid. Mech.* 577:137–59

Vitousek S, Fringer OB. 2011. Physical versus numerical dispersion in nonhydrostatic ocean modeling. *Ocean Model.* 40:72–86
Wain DJ, Gregg MC, Alford MH, Lien RC, Hall RA, Carter G. 2013. Propagation and dissipation of the internal tide in upper Monterey Canyon. *J. Geophys. Res. Oceans* 118:4855–77
Walter RK, Squibb ME, Woodson CB, Koseff JR, Monismith SG. 2014. Stratified turbulence in the nearshore coastal ocean: dynamics and evolution in the presence of internal bores. *J. Geophys. Res. Oceans* 119:8709–30
Waterman S, Naveira Garabato AC, Polzin KL. 2012. Internal waves and turbulence in the Antarctic Circumpolar Current. *J. Phys. Oceanogr.* 43:259–82
White M. 1994. Tidal and subtidal variability in the sloping benthic boundary layer. *J. Geophys. Res.* 99:7851–64
Winters KB. 2015. Tidally driven mixing and dissipation in the stratified boundary layer above steep submarine topography. *Geophys. Res. Lett.* 42:7123–30
Winters KB, Armi L. 2013. The response of a continuously stratified fluid to an oscillating flow past an obstacle. *J. Fluid Mech.* 727:83–118
Wong SH, Santoro AE, Nidzieko NJ, Hench JL, Boehm AB. 2012. Coupled physical, chemical, and microbiological measurements suggest a connection between internal waves and surf zone water quality in the Southern California Bight. *Cont. Shelf Res.* 34:64–78
Wunsch C, Ferrari R. 2004. Vertical mixing, energy, and the general circulation of the oceans. *Annu. Rev. Fluid Mech.* 36:281–314
Wunsch S. 2015. Nonlinear harmonic generation by diurnal tides. *Dyn. Atmos. Oceans* 71:91–97
Zhang HP, King B, Swinney HL. 2007. Experimental study of internal gravity waves generated by supercritical topography. *Phys. Fluids* 19:096602
Zhang HP, King B, Swinney HL. 2008. Resonant generation of internal waves on a model continental slope. *Phys. Rev. Lett.* 100:244504
Zhao Z. 2014. Internal tide radiation from the Luzon Strait. *J. Geophys. Res. Oceans* 119:5434–48

Annual Review of
Fluid Mechanics

Volume 49, 2017

Contents

Indexes

Errata

An online log of corrections to *Annual Review of Fluid Mechanics* articles may be found at http://www.annualreviews.org/errata/fluid